Supporting Information: Design of spectral-spatial phase prewinding pulses and their use in small-tip fast recovery steady-state imaging

Sydney N. Williams[1], Jon-Fredrik Nielsen[1], Jeffrey A. Fessler[2], Douglas C. Noll[1]

1. Department of Biomedical Engineering and 2. Department of Electrical Engineering and Computer Science, University of Michigan, Ann Arbor, MI, USA

This document provides additional discussion and experimental results that supplement (1).

A. Local spectral-spatial bandwidth as a model for intravoxel dephasing

Spatially varying bandwidth

Choosing a local bandwidth L to design spectral-spatial pulses faces multiple competing demands. On one hand, a wider bandwidth L might balance the competing needs of spatial resolution and pulse length, allowing the prewinding pulse to capture larger range of off-resonance. On the other hand, a wider L could increase SAR, making the RF optimization problem more challenging and lead to overall worse prewinding performance. This section explores a few design considerations for local bandwidth L and concludes that simply using a uniform L =25 Hz is sufficient for the spectral-spatial pulses designed in the paper.

One possible alternative is to adapt L to changing ΔB_0 offset based on (2), which noted that there is proportionality between off-resonance frequency $f(x, y)$ and through-plane gradient g_z. This can be expressed as

$$g_z = \alpha f(x, y) \qquad \text{[S–1]}$$

where α is the proportionality constant. In (2), α was estimated from contiguous field maps as -2.03×10^{-4} G/cm/Hz. We therefore chose to explore through-plane contributions to intravoxel bandwidth spread using $\alpha = -2 \times 10^{-4}$ G/cm/Hz. We did this by adapting the local bandwidth spatially considering through-plane gradient effects (2) by applying the following equation:

$$L_{\text{tp}}(x, y) = \gamma \alpha \Delta z |\Delta f(x, y)| \ . \qquad \text{[S–2]}$$

Here $L_{\text{tp}}(x, y)$ is the spatially varying local bandwidth attributed to the through-plane gradient, γ is the gyromagnetic ratio, and $\Delta z = 0.4$ cm was the slice thickness used in the 3D field map acquisition. We also centered the field map $\Delta f(x, y)$ to a median value of 0 Hz. Using Eq. [S–2] alone would cause spatial locations at or close to the median field map frequency to have a through-plane local bandwidth value of about 0 Hz. Furthermore, at the farthest field map deviation value of 129 Hz, Eq. [S–2] would yield $L_{\text{tp}} = 44$ Hz. We chose to balance the contribution of through-plane gradient and the original uniform $L = 25$ Hz. We associate the 25 Hz bandwidth with microscopic effects of T2* decay, whereas the through-plane dephasing proportional to ΔB_0 is related to macroscopic effects. These effects are largely independent and thus are treated as orthogonal sources of bandwidth spread. This leads to a quadrature combination, so the final spatially varying $L_{\text{total}}(x, y)$ we investigated is:

$$L_{\text{total}}(x, y) = \sqrt{(\gamma \alpha \Delta z |\Delta f(x, y)|)^2 + 25^2} \ . \qquad \text{[S–3]}$$

We then incorporated this spatially varying bandwidth into the design through the weighting matrix. To

design an RF pulse using Eq. [S–3], the weighting matrix $\mathbf{W}$ contained samples of

$$w(x,y,f) = \begin{cases} 1, & |f - \Delta f(x,y)| \leq \frac{L_{\text{total}}(x,y)}{2} \\ 0, & \text{otherwise} \ . \end{cases} \quad \text{[S–4]}$$

See Supp. Fig. S1 for an illustration that compares Eq. [S–4] (Supp. Fig. S1 bottom row) to the original fixed bandwidth design in Eq. [5] of (1) (Sup. Fig. S1 top row).

Gaussian weights in the design weighting matrix

These two implementations of $\mathbf{W}$ (spatially varying and uniform $L_{\text{total}}(x,y)$) are binary weighting matrices, where the only weight values used are 0's and 1's. We also investigated using Gaussian weights instead of binary weights in the design weighting matrix so it matches the Gaussian weight model used in calculating the performance metrics, e.g., Excitation NRMSE. In this case, the values of $w(x,y,f)$ included in the matrix are scaled to normalized Gaussian weights as

$$w(x,y,f) = \begin{cases} \frac{g(f;x,y)}{\max(g(f;x,y))}, & |f - \Delta f(x,y)| \leq 3L_{\text{total}}(x,y) \\ 0, & \text{otherwise} \end{cases} \quad \text{[S–5]}$$

where $g(f;x,y)$ is the Gaussian weight at frequency f. We define $g(f;x,y)$ as

$$g(f;x,y) = \frac{1}{L_{\text{total}}(x,y)\sqrt{2\pi}} \exp\left[-\frac{(\bar{f}(x,y) - f)^2}{2L_{\text{total}}(x,y)^2}\right] \quad \text{[S–6]}$$

where $\bar{f}(x,y)$ is the mean frequency within the $L_{\text{total}}(x,y)$ bandwidth region at location (x,y) and the standard deviation $L_{\text{total}}(x,y)$ can also be uniform or spatially varying for the Gaussian weights.

In total, we investigated the design of spectral-spatial pulses with 4 unique weighting matrices $\mathbf{W}$: binary entries (Eq. [S–4]) with i) uniform $L_{\text{total}}(x,y)$ =25 Hz intravoxel spread or ii) spatially varying spread $L_{\text{total}}(x,y)$ defined in Eq. [S–3], and Gaussian-weighted entries (Eq. [S–5]) with iii) uniform $L_{\text{total}}(x,y)$ =25 Hz intravoxel spread and 25 Hz standard deviation or iv) spatially varying spread $L_{\text{total}}(x,y)$ and spatially varying standard deviation. Supporting Figure S1 illustrates these distinct design weighting matrices. Each box of Supp. Fig. S1 represents a sampled frequency f and the plots are shown in spatial dimension x,y. To further investigate this approach, all simulation results use a finer spectral sampling rate of Δf =5 Hz (Δf =10 Hz was used in (1)).

Spatially varying standard deviation in Bloch simulation

For completeness, we also considered a refinement of the simulation methods. In (1), we used an intravoxel frequency spread in Bloch simulation spanning a [-3σ:10:3σ] Hz range, where σ =25 Hz defined the standard deviation of normalized Gaussian distribution weights $\mathbf{g}$ used to combine these simulation results. Just like we considered spatially varying intravoxel widths for $\mathbf{W}$ of our spectral-spatial pulse design, we could simulate over ranges with spatially varying standard deviation $L_{\text{total}}(x,y)$ similar to Eq. [S–3]. Hence, we now have two methods for multi-frequency Bloch simulation: normalized Gaussian weights with a uniform standard deviation and a spatially varying standard deviation.

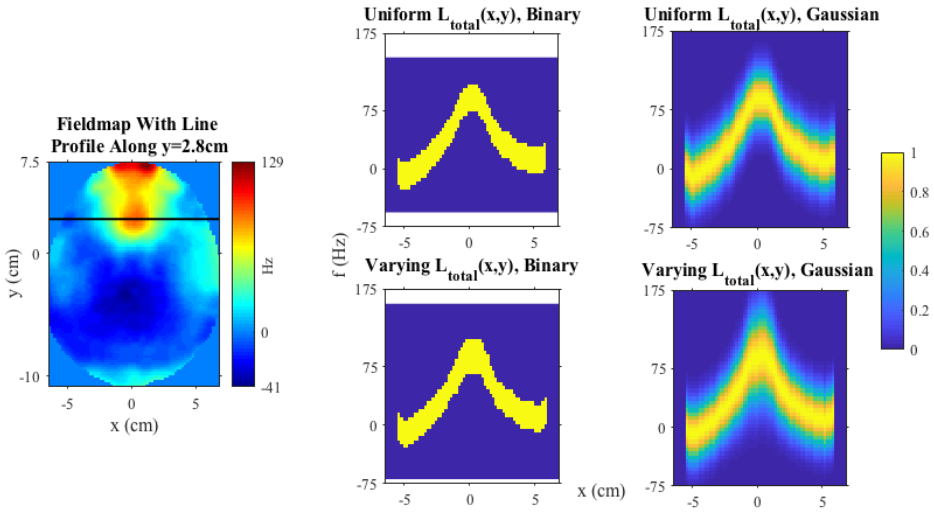

Supporting Figure S1: Four possible design weighting matrices $\mathbf{W}$ for spectral-spatial pulse prewinding. In the top row, the intravoxel bandwidth spread is universally $L_{\text{total}}(x, y)$ =25 Hz at all locations. In the bottom this value varies spatially with the spread proportional to through-plane gradient. In the left column, the values included in $\mathbf{W}$ are binary (0's or 1's). In the right column, the values are weighted by a normalized Gaussian distribution. In (1), we used the top left design weighting matrix.

Results

To facilitate our forthcoming discussion, Supporting Table S1 summarizes these design/simulation combinations and provides shorthand variable naming conventions for each possible combination of design matrix and simulation method.

		Design Weighting Matrix Method			
		Binary $\mathbf{W}$ with Uniform $L_{\text{total}}(x, y)$	Binary $\mathbf{W}$ with Varying $L_{\text{total}}(x, y)$	Gaussian $\mathbf{W}$ with Uniform $L_{\text{total}}(x, y)$	Gaussian $\mathbf{W}$ with Varying $L_{\text{total}}(x, y)$
Simulation Methods	Gaussian with Uniform Standard Deviation	$\mathbf{BU}_L\mathbf{U}_{\text{std}}$	$\text{BV}_L\text{U}_{\text{std}}$	$\text{GU}_L\text{U}_{\text{std}}$	$\text{GV}_L\text{U}_{\text{std}}$
	Gaussian with Varying Standard Deviation	$\text{BU}_L\text{V}_{\text{std}}$	$\text{BV}_L\text{V}_{\text{std}}$	$\text{GU}_L\text{V}_{\text{std}}$	$\text{GV}_L\text{V}_{\text{std}}$

Supporting Table S1: Possible combinations of design weighting matrices (columns) and simulation methods (rows) for spectral-spatial pulse design. The original method presented in the main paper is assigned the naming convention "$\mathbf{BU}_L\mathbf{U}_{\text{std}}$".

We explored designing four sets of spectral-spatial pulses (using four weighting matrix methods) and simulated their performance with both simulation methods for the fieldmap shown in Supp. Fig. S1. One of these combinations, "$\text{BU}_L\text{U}_{\text{std}}$", is used in (1) (albeit with 10 Hz rather than 5 Hz spacing for the design). Supporting Table S2 lists the performance of all 8 design/simulation combinations with the naming conventions provided in Supporting Table S1.

Design/ Simulation Method	Excitation NRMSE	Phase RMSE (°)	Mean Magnitude	% Magnitude St. Dev.	Magnitude NRMSE
$\mathrm{BU}_L\mathrm{U}_{\mathrm{std}}$	**0.18**	7.4	**0.24**	7.8	**0.14**
$\mathrm{BV}_L\mathrm{U}_{\mathrm{std}}$	**0.18**	**7.0**	**0.24**	**7.0**	**0.14**
$\mathrm{GU}_L\mathrm{U}_{\mathrm{std}}$	0.29	8.0	0.20	7.8	0.26
$\mathrm{GV}_L\mathrm{U}_{\mathrm{std}}$	0.32	8.1	0.20	11.1	0.31
$\mathrm{BU}_L\mathrm{V}_{\mathrm{std}}$	0.21	8.8	**0.24**	11.4	0.17
$\mathrm{BV}_L\mathrm{V}_{\mathrm{std}}$	0.21	8.0	**0.24**	9.9	0.17
$\mathrm{GU}_L\mathrm{V}_{\mathrm{std}}$	0.31	9.8	0.20	10.4	0.28
$\mathrm{GV}_L\mathrm{V}_{\mathrm{std}}$	0.33	9.3	0.20	12.5	0.31

Supporting Table S2: Performance metrics of all possible design weight matrix/simulation methods tested. The first row "$\mathrm{BU}_L\mathrm{U}_{\mathrm{std}}$" represents the weighting design matrix and simulation method used in (1). The bold values represent the best performance.

We expected the performance metrics, particularly excitation NRMSE and phase RMSE, to worsen when simulation methods went from using a Gaussian spread of intravoxel frequencies with uniform standard deviation σ to a spatially varying spread where σ increased at areas of higher off-resonance due to through-plane effects. Supporting Table S2 shows where performance drops slightly from design/simulation combinations ending in "$\mathrm{XXU}_{\mathrm{std}}$" to "$\mathrm{XXV}_{\mathrm{std}}$". It was harder to predict how adjusting the design weighting matrix would affect the spectral-spatial pulse performance. Supporting Table S2 reports decreases in performance for design weighting matrices when adjusting from binary to Gaussian weight values ("BXX" to "GXX"). There are negligible differences when comparing uniform and varying $L_{\mathrm{total}}(x, y)$ in the weight matrix ("X$U_L X$" to "XV_LX"). This is likely because changing the design weight matrix from binary to Gaussian weights increases the support of $\mathbf{W}$ in the frequency dimension, resulting in a more challenging RF design. The magnitude simulation images (Supp. Fig. S2) and phase simulation images (Supp. Fig. S3) are visually consistent with the fact that the various design alternatives yield similar results but with a slight decline for some explored methods for this particular slice.

In conclusion, we explored modifying the weighting matrix used in designing spectral-spatial pulses by i) varying the design target bandwidth $L_{\mathrm{total}}(x, y)$ to reflect the proportionality between off-resonance and through-plane gradient using references such as (2) and ii) varying the weights of the design weighting matrix to be Gaussian rather than binary. We also went further and investigated simulation methods where we varied the standard deviation of the Gaussian intravoxel spread of frequencies to be spatially varying with off-resonance. After testing all possible combinations, we saw only small changes in simulation performance metrics. It is possible that with higher spatial resolution excitation k-space trajectories we might see greater gains with these modifications. However, this would also mean a longer RF pulse, so the potential advantages of these changes is unclear.

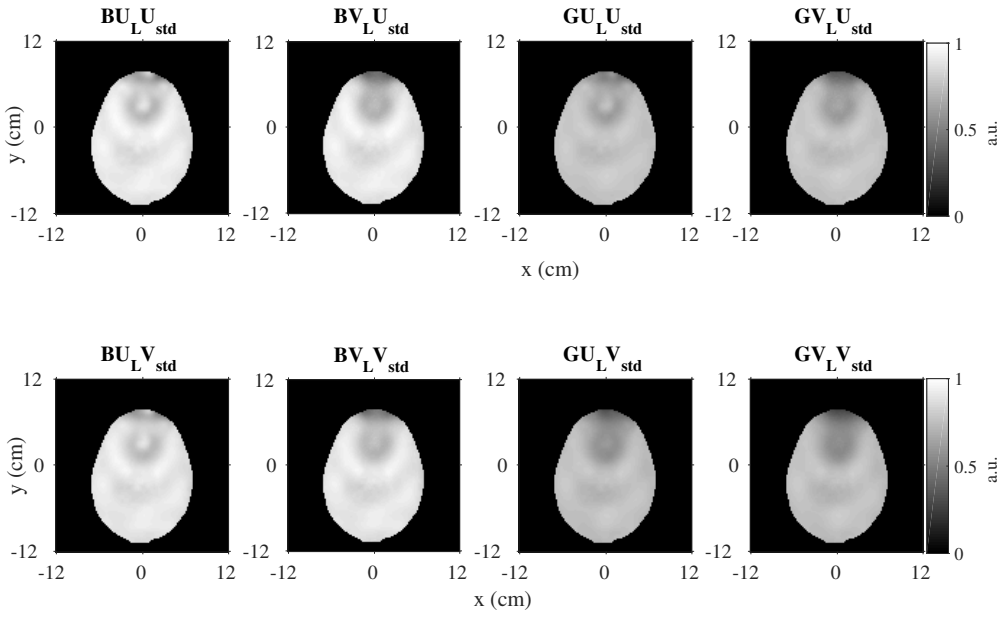

Supporting Figure S2: Simulated magnitude images for all possible design weighting matrix and simulation combinations presented in Table S1.

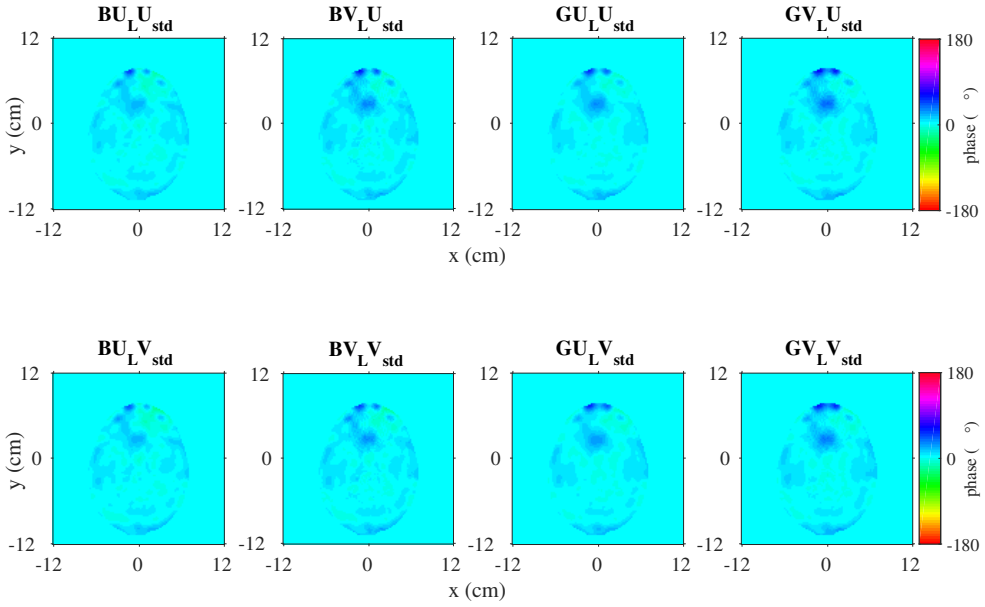

Supporting Figure S3: Simulated phase images for all possible design weighting matrix and simulation combinations presented in Table S1.

B. Hard pulse simulation and prewinding pulse performance over one frequency and one spatial dimension

In (1) we compare spectral and spectral-spatial prewinding pulses, building on previous work in (3) and (4). In this supporting information, we also compare these to the performance of a non-prewinding pulse. In this case, we simulate a simple 500 μs hard rect pulse that has the same TE and flip angle as our human spectral and spectral-spatial RF pulse designs (3.648 ms/ 16°). Supporting Table S3 below reports performance metrics (Eq. [7-11] in main paper) for this hard pulse and the spectral and spectral-spatial pulses. As expected, the hard pulse has a uniform magnetization appearance but does not reach the target magnitude (% magnitude standard deviation, magnitude NRMSE) and fails to acheive a flat phase profile since no prewinding has occured (phase RMSE, excitation NRMSE).

Pulse	Excitation NRMSE	Phase RMSE (°)	Mean Magnitude	% Magnitude St. Dev.	Magnitude NRMSE
Hard pulse	0.64	43.5	**0.24**	**0.1**	**0.13**
Purely spectral pulse	0.54	25.2	0.17	19.6	0.39
Spectral-spatial pulse	**0.18**	**7.0**	**0.24**	7.7	0.15

Supporting Table S3: Performance metrics defined in paper as (Eq. [7-11]) for a simulated hard pulse in comparison to purely spectral and spectral-spatial prewinding pulses. The bold values represent the best performance.

In addition to the performance metrics provided, we have created plots to demonstrate the performance of prewinding pulses as a function of one spatial dimension and frequency before summation using Gaussian weights. To do this, we selected a particular "y" location in the 2D in vivo field map and drew a line profile spanning all "x" through it. We then examined the magnetization of both purely spectral and spectral-spatial pulses across this line profile for all frequencies included in Bloch simulation. Finally, we repeated this same process for one "x" location and the corresponding "y" line profile.

Supporting Figure S4 shows the magnetization simulations for one spatial dimension and all simulation frequencies for the hard pulse. The simulations are presented in terms of relative complex error ($|\frac{m_{xy}}{\sin\alpha} - 1|$), absolute phase error ($|\angle m_{xy}|$), and relative magnitude error ($|\frac{|m_{xy}|}{\sin\alpha} - 1|$). This diagram also shows the 2D human field map, simulated magnitude, and simulated phase over all combined frequencies using a Gaussian distribution with σ =25 Hz as described in the main paper. Supporting Figures S5 and S6 repeat these plots for the purely spectral and spectral-spatial pulse, respectively.

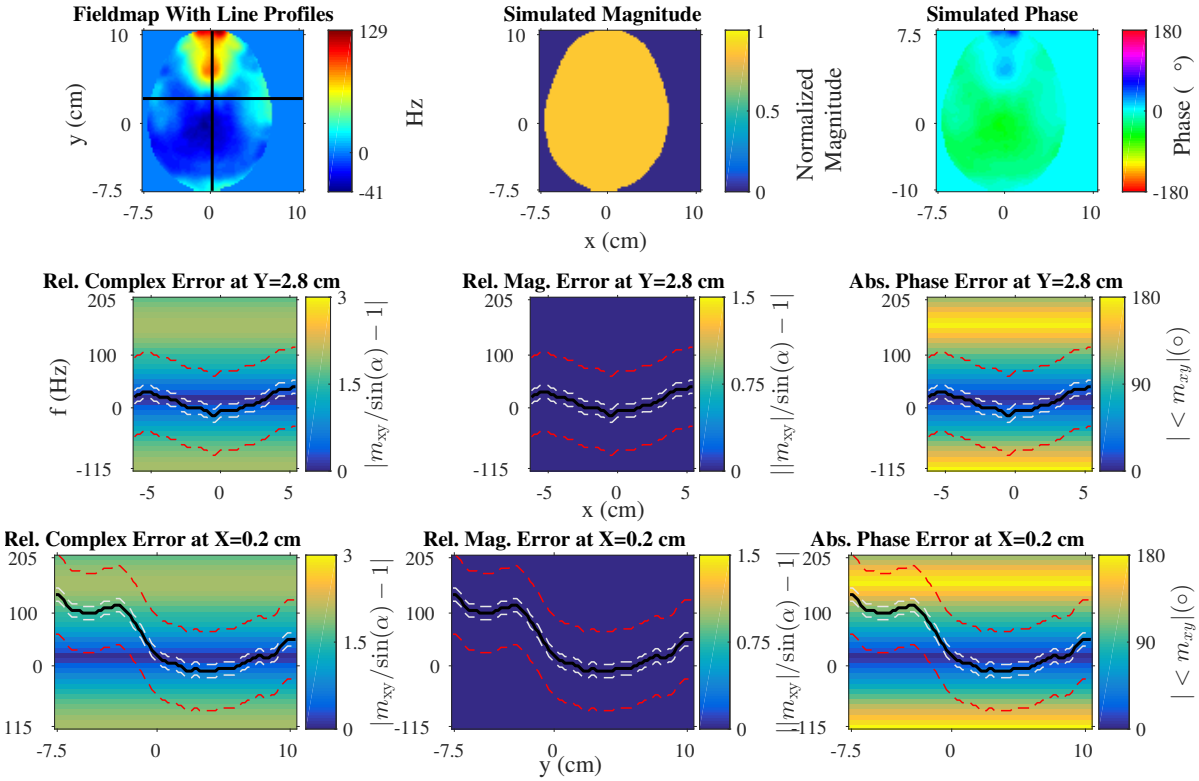

Supporting Figure S4: Hard pulse simulation results. Top row: 2D field map (left), simulated magnitude (center), and simulated phase (right). Middle row: relative complex error, relative magnitude error, and absolute phase error for the 1D line profile magnitude across all x at y =2.8 cm. Bottom row: relative complex error, relative magnitude error, and absolute phase error for profile across all y at y =0.2 cm. The dashed white lines represent the L =25 Hz used as the local bandwidth for the spectral spatial pulse, and the dashed red lines represent the $\pm 3\sigma = 75$ Hz bandwidth used in Bloch simulation. These plots are repeated for the spectral and spectral-spatial pulses in Supp. Figs S5 and S6.

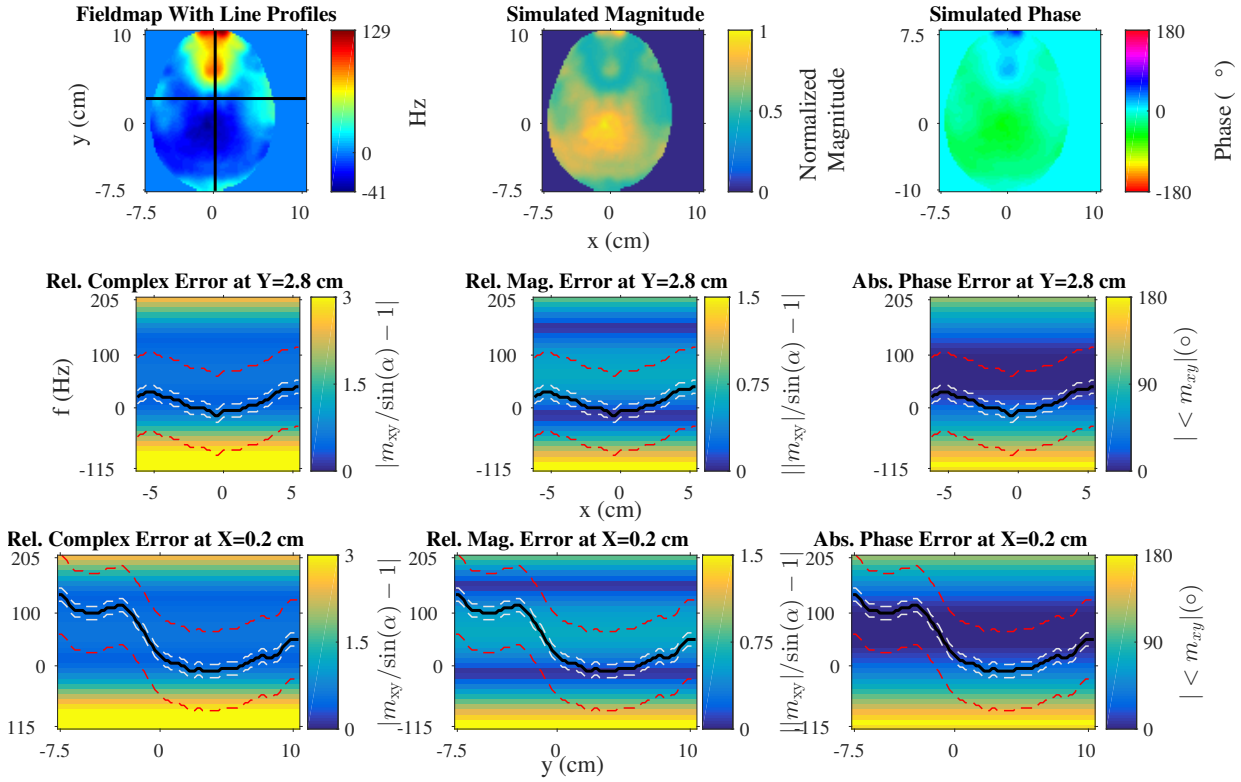

Supporting Figure S5: Purely spectral pulse simulation results. Compare with Supp. Figs S4 and S6.

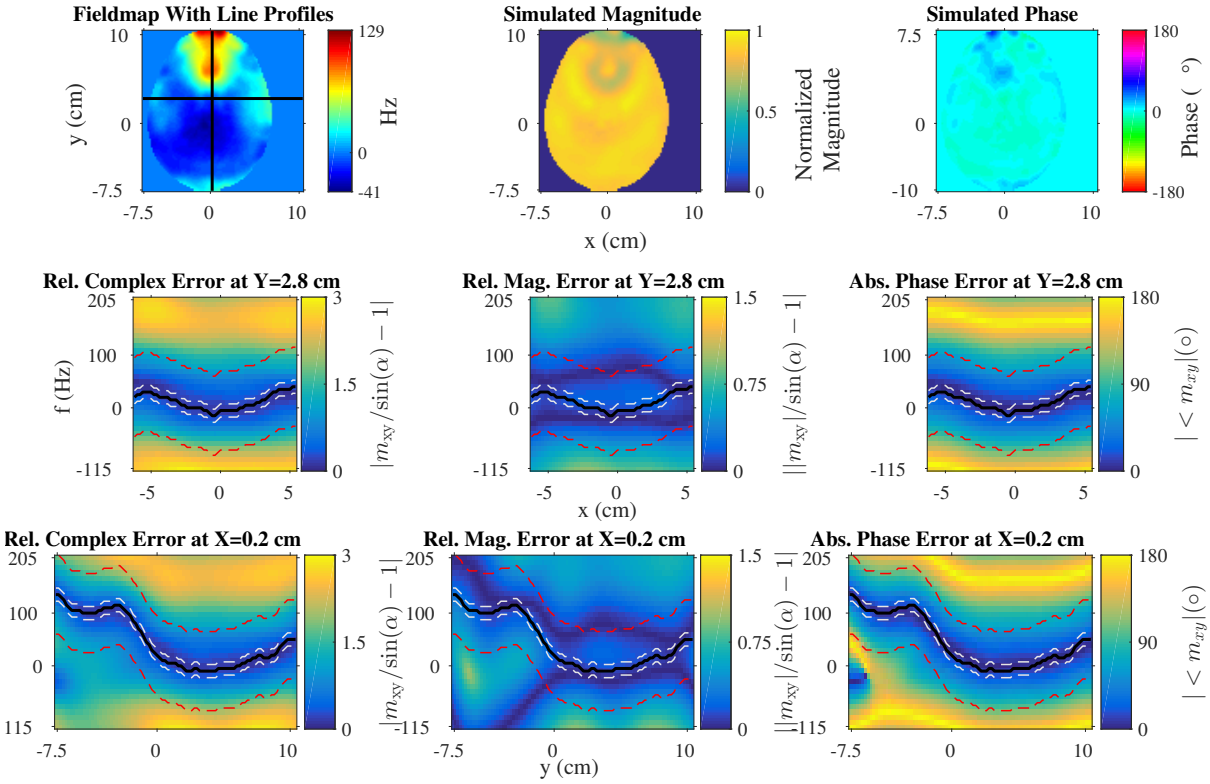

Supporting Figure S6: Spectral-spatial pulse simulation results. Compare with Supp. Figs S4 and S5.

The hard pulse plots in Supp. Fig. S4 agree with the performance metrics in Supporting Table S3 in that the pulse performs poorly with large absolute phase error and relative magnitude and complex error across all space. As anticipated, the spectral-spatial pulse in Supp. Fig. S6 tracks the spatially varying off-resonance while the purely spectral pulse in Supp. Fig. S5 does not. The purely spectral pulse has low phase error values for some spatial locations, but with varying off-resonance it cannot enforce low relative complex at all frequencies. Meanwhile, the spectral-spatial pulse maintains particularly low relative complex error with spatial variation. We therefore conclude that both effective magnitude *and* phase performance (in other words, the relative complex error) is what leads to effective prewinding. The summed frequency simulation of these three pulses in the 2D simulated magnitude and phase images are consistent with these performance differences as well.

Additional intuition about pulse performance can be gained by plotting "error" as a function of spatial location. Figure 7 in the main paper shows excitation and phase root squared error combined across all simulated frequencies as a function of spatial location for the purely spectral pulse and spectral-spatial pulse. There, we can easily see that the hard pulse performs very poorly, the spectral pulse performs moderately well, and the spectral-spatial pulse performs has the lowest phase errors.

References

[1] Williams SN, Nielsen J-F, Fessler JA, and Noll DC. Design of spectral-spatial phase prewinding pulses and their use in small-tip fast recovery steady-state imaging Magn Res Med (submitted).

[2] Yip C, Yoon D, Olafsson V, Lee S, Grissom WA, Fessler JA, Noll DC. Spectral-spatial pulse design for through-plane phase precompensatory slice selection in T_2^*-weighted functional MRI. Magn Res Med 2009;61:1137–47.

[3] Assländer J, Glaser SJ, Hennig J. Spin echoes in the regime of weak dephasing. Magn Res Med 2016; 75:150–160.

[4] Sun H, Fessler JA, Noll DC, Nielsen JF. Balanced SSFP-like steady-state imaging using small-tip fast recovery (STFR) sequence with a spectral pre-winding pulse. Magn Res Med 2016;75:839–844.